Realization of U(1) Dirac Quantum Spin Liquid in $YbZn_2GaO_5$

Sijie Xu,[1,*] Rabindranath Bag,[1,*] Nicholas E. Sherman,[2,3] Lalit Yadav,[1] Alexander I. Kolesnikov,[4] Andrey A. Podlesnyak,[4] Joel E. Moore,[2,3] and Sara Haravifard[1,5,†]

[1]*Department of Physics, Duke University, Durham, North Carolina 27708, USA*
[2]*Department of Physics, University of California, Berkeley, California 94720, USA*
[3]*Materials Sciences Division, Lawrence Berkeley National Laboratory, Berkeley, California 94720, USA*
[4]*Neutron Scattering Division, Oak Ridge National Laboratory, Oak Ridge, Tennessee 37831, USA*
[5]*Department of Mechanical Engineering and Materials Science, Duke University, Durham, North Carolina 27708, USA*

(Dated: June 1, 2023)

arXiv:2305.20040v1 [cond-mat.str-el] 31 May 2023

The emergence of a quantum spin liquid (QSL), a state of matter that can result when electron spins are highly correlated but do not become ordered, has been the subject of a considerable body of research in condensed matter physics [1]. Spin liquid states have been proposed as hosts for high-temperature superconductivity [2] and can host topological properties with potential applications in quantum information science [3]. The excitations of most quantum spin liquids are not conventional spin waves but rather quasiparticles known as spinons, whose existence is well established experimentally only in one-dimensional systems; the unambiguous experimental realization of QSL behavior in higher dimensions remains challenging. Here we investigate the novel compound $YbZn_2GaO_5$, which hosts an ideal triangular lattice of effective spin-1/2 moments with no inherent chemical disorder. Thermodynamic and inelastic neutron scattering (INS) measurements performed on high-quality single crystal samples of $YbZn_2GaO_5$ exclude the possibility of long-range magnetic ordering down to 60 mK, demonstrate a quadratic power law for the heat capacity and reveal a continuum of magnetic excitations in parts of the Brillouin zone. Both low-temperature thermodynamics and INS spectra suggest that $YbZn_2GaO_5$ is a U(1) Dirac QSL with gapless spinon excitations concentrated at certain points in the Brillouin zone, and additional features in INS are also consistent with theoretical expectations for a Dirac QSL on the triangular lattice.

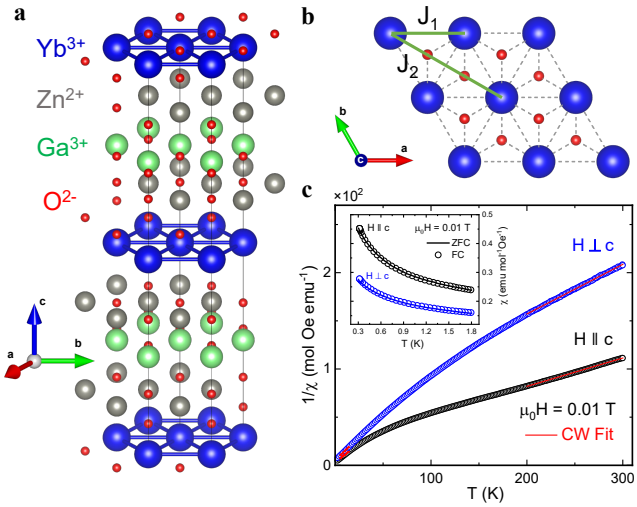

FIG. 1. **Crystal structure and magnetic susceptibility a**. Crystal structure of $YbZn_2GaO_5$; Yb-O planes are well separated by non-magnetic Zn-O, Ga-O, and Zn-O layers along crystallographic c-direction. **b**. The Yb^{3+} (blue sphere) forms a triangular lattice. The nearest neighbor couplings J_1 and next-nearest neighbor couplings J_2 are shown by green solid lines. **c**. The inverse magnetic susceptibility, $1/\chi$ (H$\|c$ and H$\perp c$) data collected on single crystal sample of $YbZn_2GaO_5$ from 2 to 300 K. The red solid lines are the Curie-Weiss (CW) Fit at the low-temperature range from 5 - 15 K and at high-temperature range from 200 - 300 K. The inset shows no splitting between zero-field-cooling (ZFC) and field cooling (FC) magnetic susceptibility data of $YbZn_2GaO_5$ crystal down to 0.3 K. The measurements were conducted under an applied magnetic field of 0.01 T parallel and perpendicular to crystallographic c - direction.

INTRODUCTION

Anderson's proposal in 1973 ignited a surge of both experimental and theoretical efforts to identify the origins and properties of QSL states [4]. QSLs are exotic states of matter that remain disordered due to strong quantum fluctuations even at ultra-low temperatures [1, 5]. Despite significant experimental efforts, the unambiguous realization of a QSL state in the real world remains a challenge. In recent years, two-dimensional triangular lattice systems with rare-earth ions carrying effective spin-1/2 moments have presented promising opportunities in realizing QSL states, given the presence of spin-orbit coupling, crystal electric fields, and strong quantum fluctuations. Among these systems, the Yb-based $YbMgGaO_4$ has been intensively studied due to the absence of magnetic ordering and the observed continuum-like inelastic neutron scattering (INS) spectra, making it a promising candidate for QSL[6–12]. However, the presence of chemical disorder in $YbMgGaO_4$, caused by the inherently mixed occupancies of magnesium and gallium atoms on the same crystallographic site, has made the interpretation of the results challenging [11–13]. Specifically, a theoretical study suggests that the chemical disorder may imitate the continuous INS spectra [11]. Further studies on a sister compound, $YbZnGaO_4$, have proposed the presence of a spin-glass ground state attributed

to the coexistence of chemical disorder and quantum fluctuation [14]. Therefore, eliminating chemical disorder and accessing the intrinsic physics of an ideal triangular lattice of effective spin-1/2 moments is highly desired. As such, a potential candidate for hosting a QSL state is another class of Yb-based triangular lattice rocksalt-type compounds that do not have significant intrinsic chemical disorder: $AYbX_2$ (A = Li, Na, K, Rb, Cs and X = O, S, Se) [15–25]. Nevertheless, the task of obtaining high-quality single-crystal samples for this particular family has posed significant challenges. As a result, most of the reported results have been derived from powder samples or small single crystals, rendering the interpretation of data quite challenging. Furthermore, it is worth noting that in this compound family, the inter-layer Yb-Yb distance is relatively shorter, which introduces a more three-dimensional magnetic structure. Thus, the crucial step toward unraveling the enigma of the QSL state in these systems lies in the design and synthesis of single crystal samples for a novel class of Yb-based triangular lattice compounds that lack intrinsic chemical disorder and exhibit quasi-two-dimensional magnetic structures.

To that end, we present a new Yb-based compound, $YbZn_2GaO_5$, that features an ideal triangular lattice of effective spin-1/2 moments without any intrinsic chemical disorder. Experiments aimed at elucidating the nature of the possible triangular lattice QSL in $YbZn_2GaO_5$ are of great importance. Thus, we grew a large and high-quality single crystal of $YbZn_2GaO_5$ (see Fig. S1) using the optical floating-zone technique to facilitate such experiments. Our heat capacity measurements indicate that at ultra-low temperatures, the heat capacity displays a $\sim T^2$ dependence, indicating a U(1) Dirac QSL behavior [26, 27]. In addition to the heat capacity measurements, we conducted an INS investigation on $YbZn_2GaO_5$ which reveals gapless, continuum-like spectra at the high-symmetry M and K points, but not throughout the Brillouin zone, and in particular not at the Γ point. This particular pattern of low-energy spinon excitations is expected for the U(1) Dirac QSL phase [28, 29] and not for a spinon Fermi surface state. Hence the heat capacity scaling and INS spectra independently are best explained by low-energy spinon excitations with Dirac-like spectrum.

RESULTS & DISCUSSION

Before discussing the results further, we would like to review briefly the key signatures that differentiate a spinon Fermi surface state from a U(1) Dirac spin liquid. First, let us start with the spinon Fermi surface state. In such a state, the low temperature heat capacity is predicted to scale as $\sim T$ [30] at the mean-field level, possibly becoming $T^{2/3}$ if emergent gauge fluctuations dominate. As for the spectrum, mean-field theory predicts a V-shape spectrum near the Γ point and gapless excitations throughout the entire Brillouin zone [5, 9, 31]. These signatures have been observed in $YbMgGaO_4$ [9, 32], and $NaYbSe_2$ [20]. For the U(1) Dirac spin liquid, the heat capacity is expected to scale as $\sim T^2$ because of the Dirac nodes [26, 33]. The low-energy theory on the triangular lattice is quantum electrodynamics (QED_3) with 4 Dirac fermions ($N_f = 4$), which predicts gapless excitations at both the M and K wavevectors [34]. The main signature to distinguish this from a spinon Fermi surface state is the presence of a gap away from these points, such as near the Γ point, as observed in recent simulations of the $J_1 - J_2$ Heisenberg model on the triangular lattice [28, 29].

Returning to the discussion of $YbZn_2GaO_5$, we demonstrate in Fig. 1a the hexagonal crystal structure of $YbZn_2GaO_5$, with the space group $P6_3mmc$. This is in contrast to $YbMgGaO_4$ and $YbZnGaO_4$ which crystallize in the $R\bar{3}m$ space group. In $YbZn_2GaO_5$, the $P6_3mmc$ space group provides unique Wyckoff positions for gallium and zinc, therefore, $YbZn_2GaO_5$ does not display any intrinsic chemical site mixing. The phase purity of our sample is confirmed through a Rietveld refinement analysis performed on the powder X-ray diffraction pattern obtained from a crushed $YbZn_2GaO_5$ single crystal (see Fig. S1). We further performed the single-crystal X-ray diffraction measurement on $YbZn_2GaO_5$ crystal and observed no discernible chemical disorder within the limit of our experimental accuracy (see Table S1). It is noteworthy to add that in $YbZn_2GaO_5$, an additional non-magnetic Zn-O layer is introduced along the crystallographic *c*-direction, which increases the distance between magnetic Yb-O planes from 8.38$\AA$ ($YbZnGaO_4$) to 10.98$\AA$, enhancing the two-dimensionality and quantum fluctuations in this compound compared to previously reported Yb-based triangular lattice QSL candidates [10, 14–16]. The nearest neighbor Yb^{3+} ions are arranged in a perfect triangular pattern with a distance of 3.37$\AA$ between them, as illustrated in Fig. 1b. This distance is comparable to that in the previously reported Yb-based triangular lattice compounds proposed to host QSL state [6, 7].

We illustrate in Fig. 1c the temperature-dependent magnetic susceptibility data collected on the single crystal of $YbZn_2GaO_5$ along both directions parallel and perpendicular to the crystallographic c-axis, in the presence of an applied magnetic field of 0.01 T. The inset of Fig. 1c highlights the low-temperature susceptibility region down to 0.3 K, confirming the absence of magnetic ordering down to this temperature. The inverse magnetic susceptibility data are fitted to Curie-Weiss law: $1/\chi = (T - \theta_{CW})/C$, (where θ_{CW} is the Curie-Weiss temperature, and C is the Curie constant) at two different temperature regimes. The obtained effective moment ($\mu_{eff} \simeq 4.36\ \mu_B$) at a high-temperature range agrees with the expected theoretical value of free Yb^{3+} ion ($\simeq 4.54\ \mu_B$). The Curie-Weiss temperatures obtained for $YbZn_2GaO_5$ in the low-temperature range (5 - 15 K) are slightly higher ($\theta_{CW,\parallel}$ = - 3.77 K and $\theta_{CW,\perp}$ = - 5.22 K) than those of Yb(Mg, Zn)GaO_4 [6, 7, 9, 14, 35]. This observation suggests a stronger antiferromagnetic coupling between Yb^{3+} ions in $YbZn_2GaO_5$. The collected isothermal magnetization data along both directions up to 14 T of applied magnetic field provides anisotropic Landé-g factors ($g_\parallel \simeq 3.44$ and $g_\perp \simeq$

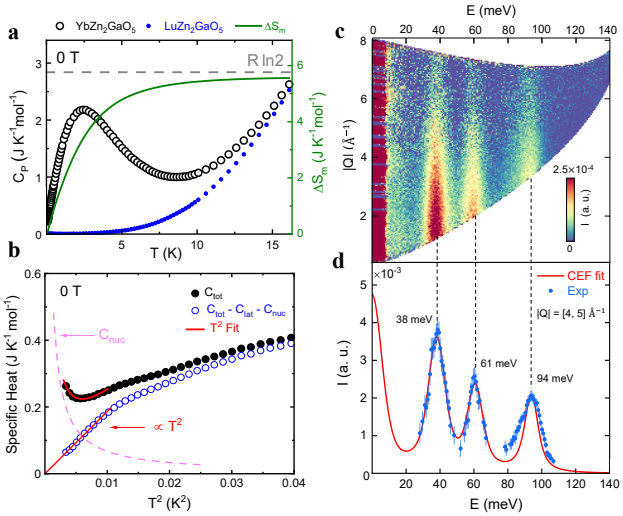

FIG. 2. **Heat capacity and crystal electric field levels.** **a**. Heat capacity data of $YbZn_2GaO_5$ single crystal and $LuZn_2GaO_5$ powder sample collected under zero field and down to 0.06 K are shown. The calculated magnetic entropy (right Y-axis) of $YbZn_2GaO_5$ saturates to Rln2, indicating the effective spin-1/2 ground state. **b**. Heat capacity vs T^2 plot: Low-temperature total heat capacity ($C_{tot} = C_{lat} + C_{nuc} + C_{mag}$) shows an upturn below 0.1 K. Using an isostructural nonmagnetic $LuZn_2GaO_5$ and a fitted Schottky model ($C_{nuc} \simeq AT^{-2}$), the lattice and nuclear contributions were removed. The magnetic heat capacity data (C_{mag}) after subtraction is presented as open circles and fitted with a solid red straight line that exhibits a quadratic T-dependence ($C_{mag} \simeq \gamma T^2$). The quadratic T-dependence fit yields an adjusted R-square value of 0.9583, indicating excellent agreement between the model and experimental data. The T^2 dependency of magnetic heat capacity data for T $\rightarrow$ 0 implies $YbZn_2GaO_5$ is a U(1) Dirac QSL candidate. **c** Inelastic neutron scattering (INS) spectra of $YbZn_2GaO_5$ reveal three crystal electric field (CEF) bands. The phononic contribution is subtracted using an isostructural nonmagnetic sample $LuZn_2GaO_5$.**d** The single-ion CEF fitting shows energy levels at 38 meV, 61 meV, and 94 meV.

3.04), which are found to be in agreement with those reported earlier for $YbZnGaO_4$ [14] (see Fig. S1).

We show in Fig. 2a zero-field heat capacity measurement performed on $YbZn_2GaO_5$ single crystal sample down to 0.06 K, confirming the absence of any long-range magnetic ordering. The contribution of phonons is subtracted using the isostructural non-magnetic sample of $LuZn_2GaO_5$. In Fig. 2b, we highlight the low-temperature behavior of the heat capacity data below 0.2 K, which is particularly intriguing. The heat capacity of $YbZn_2GaO_5$ at low temperature has multiple contributions denoted by $C_{tot} = C_{lat} + C_{nuc} + C_{mag}$. C_{lat} represents the lattice (phononic) contribution that is negligible below 0.1 K. C_{nuc} accounts for the nuclear Schottky contribution due to the hyperfine splitting of the nuclear energy levels resulting from the interaction between nuclear spins and electrons [36]. The nuclear contribution ($C_{nuc} \simeq AT^{-2}$) is subtracted by fitting the heat capacity data below 0.1 K and the fitting coefficient value (A = 6.72(4)$\times$ 10^{-4} JKmol^{-1}) is consistent with that reported for other Yb-based compounds [21]. The subtracted magnetic heat capacity data (C_{mag}) displays a $\sim T^2$ dependence (red solid straight line in Fig. 2b) with a coefficient of $\gamma = C_{mag}/T^2 = 18.6(1)$ JK^{-3}mol^{-1} below 0.1 K. We also attempted to fit the magnetic heat capacity data with a linear dependence ($C_{mag} \sim T$), but this fitting approach did not provide a satisfactory result (see Fig. S3). The magnetic heat capacity data exhibiting a $\sim T^2$ dependence for T $\rightarrow$ 0 and the lack of any long-range magnetic ordering down to the lowest temperature of 0.06 K imply that the ground state of $YbZn_2GaO_5$ is a U(1) Dirac QSL candidate [26, 33].

To obtain a better understanding of the ground state of $YbZn_2GaO_5$, an INS experiment was conducted on a high-purity powder sample at 5 K, as shown in Fig. 2c,d. The single-ion crystal electric field (CEF) fitting results revealed three distinct crystal field excitations at 38 meV, 61 meV, and 94 meV, which agree with those observed in other previously reported Yb-based triangular lattice systems [13, 16, 20, 37–39]. Based on our analysis of the CEF levels, we have determined that the first excited state of $YbZn_2GaO_5$ is separated from the ground state by a gap of over 441 K (38 meV). This suggests a Kramer's doublet ground state for the Yb^{3+} ions with an effective spin-1/2. Our CEF fitting scheme, which is consistent with the heat capacity data, supports this conclusion. In particular, the calculated magnetic entropy of $YbZn_2GaO_5$ saturates at Rln2, indicating an effective spin-1/2 ground state, as shown in Fig. 2a (see Tables S2 and S3 for further details on the CEF fitting scheme).

Furthermore, we conducted INS experiments on a high-quality single crystal of $YbZn_2GaO_5$. These experiments were designed to probe the low-energy excitations of the material. An incident neutron energy of 3.32 meV was used and the excitation spectrum under zero-field was collected at a base temperature of 0.1 K. Scans performed at a high temperature of 45 K were used for background subtraction (see Fig. S2). We show in Fig.3a the scattering intensity as a function of energy transfer, with a path taken through the high-symmetry points of K_1-M_1-K-Γ_1/Γ_2-K-M_2-K_2, as illustrated in Fig.3c. A broad continuum extending over an energy scale of approximately 1.4 meV was observed, with the spectrum weight gradually decreasing at higher energy. We observed a clear gap in the spectra of $YbZn_2GaO_5$ near the Γ point, while the excitation remained gapless between M and K points within the instrumental energy resolution of approximately 0.06 meV, as shown in Fig. 3a. Our theoretical calculation, which is based on the J_1-J_2 XXZ model (See the Methods section for details) and uses large-scale matrix product state simulations [28], shows promising agreement with our experimental data, with J_2/J_1 = 0.12 and an anisotropy value of Δ = 1.35 (see Fig. 3b). In contrast to $YbZn_2GaO_5$, other reported Yb-based triangular systems, such as the delafossite material $NaYbSe_2$, display a continuum spectrum without a gap at all Q. This observation is consistent with a spinon Fermi surface state [20, 31]. However, in $YbZn_2GaO_5$, the observed energy gap near Γ along with the gapless continuum spectra observed at Q = K and M are indicative of a U(1) Dirac QSL state [28].

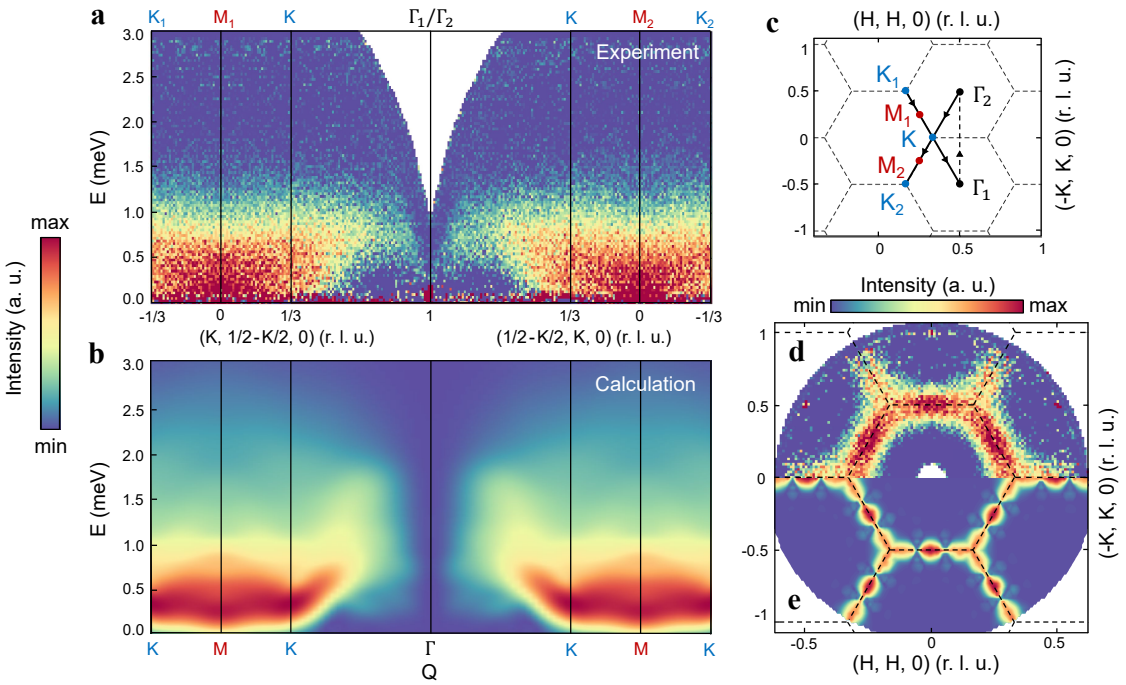

FIG. 3. **Inelastic Neutron scattering data under zero applied magnetic field a**. Energy dependence of the magnetic excitation spectrum along high symmetry points measured at 0.1 K. The background is subtracted using the high temperature (45 K) spectrum (See Methods section for details). The contour path travels along the high symmetry points K_1-M_1-K-Γ_1/Γ_2-K-M_2-K_2, which is illustrated by the black solid curve in c. **b**. Calculated spectrum using matrix product states for the $J_1 - J_2$ XXZ model on the triangular lattice, with $J_2/J_1 = 0.12$ and $\Delta = 1.35$ (see Methods section for details). We use J_1 = 0.5 meV to adjust the scale of the y-axis for better comparison of the experimental data. **c**. A schematic of the high symmetry path used in a,b. The dashed lines show the boundary of the Brillouin zones. **d**. Background-subtracted low energy slice of the magnetic excitation spectrum collected at 0.1 K. The energy integration range is [0.1, 0.3] meV. **e**. The calculated spectrum of the $J_1 - J_2$ XXZ model with the same parameters as in b. We integrate the spectrum in the energy range [0.1, 0.3] meV for comparison with d.

The thermodynamics measurements are consistent with this spectrum, as the magnetic heat capacity data (C_{mag}) exhibits a $\sim T^2$ dependence for T $\rightarrow$ 0, which is also indicative of a U(1) Dirac QSL.

In Fig. 3d, we demonstrate the experimental dispersion of the neutron scattering intensities through constant energy slice integrated from 0.1 to 0.3 meV. We observe that at low energy, spectral weights are localized at the edge of the Brillouin zone, with higher intensities at the M points than at the K points. As the energy increases, the difference in intensities between M and K points becomes less prominent, and the intensities disperse throughout the Brillouin zone, as shown in Fig. S5. Moreover, the theoretical calculations in Fig. 3e agree with our experimental observations in similar energy ranges. The agreement between theory and experiment suggests that INS spectra of $YbZn_2GaO_5$ are sufficiently well described by the $J_1 - J_2$ XXZ model without additional couplings. The presence of gapless modes at K and M while having a gap near Γ strongly favors a U(1) Dirac QSL ground state over either a spinon Fermi surface or the effects of disorder.

CONCLUSIONS

In conclusion, we have successfully synthesized and characterized high-quality single crystals of $YbZn_2GaO_5$, a Yb-based triangular lattice system without any intrinsic chemical disorder. Our experiments reveal that the magnetic heat capacity data at ultra-low temperatures follow a T^2 dependence, providing experimental evidence for the realization of U(1) Dirac QSL on a triangular lattice in $YbZn_2GaO_5$. Additionally, our INS investigation of $YbZn_2GaO_5$ demonstrates gapless, continuum-like spectra at the high-symmetry M and K points but *not* at the Γ point, confirming the possibility of a U(1) Dirac QSL ground state in this compound. Our experimental results are supported by theoretical interpretations. Therefore, we suggest that $YbZn_2GaO_5$ is a highly promising candidate for the long-sought U(1) Dirac QSL and warrants further investigations with other techniques.

ACKNOWLEDGEMENTS

We would like to express our gratitude to Sachith E. Dissanayake and Cristian D. Batista for their valuable contribu-

tions to our discussions. We are thankful to Chun-Hsing Chen and the X-ray Core Laboratory of the Department of Chemistry at the University of North Carolina at Chapel Hill for their help with single-crystal X-ray diffraction measurements. Work performed at Duke University is supported by the U.S. Department of Energy, Office of Science, Office of Basic Energy Sciences, under Award Number DE-SC0023405. Work performed at the University of California, Berkeley, is supported by the U.S. Department of Energy, Office of Science, National Quantum Information Science Research Centers, Quantum Science Center. N.S. is additionally supported by the Theory Institute for Materials and Energy Spectroscopies (TIMES) of the U.S. Department of Energy, Office of Basic Energy Sciences, under contract DE-AC02-05CH11231. R.B. acknowledges the support provided by Fritz London Endowed Post-doctoral Research Fellowship. This research used resources of the Spallation Neutron Source at Oak Ridge National Laboratory, which is a DOE Office of Science User Facility.

AUTHOR CONTRIBUTIONS

Research conceived by S.H.; Samples synthesized by S.X., R.B., and S.H.; Magnetic measurements performed and analyzed by S.X., R.B., and S.H.; Heat capacity measurements performed and analyzed by S.X., R.B, and S.H.; Neutron scattering measurements performed and analyzed by S.X., A.I.K., A.A.P, and S.H.; Theoretical calculations performed by N.E.S. and J.E.M.; Manuscript written by S.X., R.B., N.E.S., J.E.M., and S.H.; All authors commented on the manuscript.

METHODS

Sample preparation and single crystal growth

The poly-crystalline sample of $YbZn_2GaO_5$ was synthesized using a solid-state reaction route. The high-purity precursors of Yb_2O_3 (99.9%), Ga_2O_3 (99.9%), and ZnO (99.9%) with 5% excess ZnO were used and mixed thoroughly and then pressed into a pellet. The pellets were sintered at 1275 ℃ for 36 hours with intermediate grinding to obtain a pure phase of $YbZn_2GaO_5$. The phase purity is confirmed using Powder X-ray diffraction (PXRD) (see Fig. S1). The pure powder sample and around 10% excess of ZnO were mixed and pressed into a cylindrical rod using a hydrostatic pressure of 700 bar. Single crystals of $YbZn_2GaO_5$ were grown using the optical floating-zone technique in the presence of a 10-bar oxygen atmosphere. A transparent single-grain crystal was successfully obtained, with a cleaved facet plane along [001] which was confirmed from Laue X-ray diffraction (see Fig. S1).

Single crystal X-ray diffraction

The single crystal X-ray diffraction (SCXRD) is performed on $YbZn_2GaO_5$ single crystal sample at the Department of Chemistry, University of North Carolina. A colorless transparent crystal piece (approximate dimensions $0.020 \times 0.010 \times 0.010\, mm^3$) was harvested by an X-ray transparent loop made by MiTeGen and mounted on a Bruker D8 VENTURE diffractometer and measured at 150 K. The data collection was carried out using Mo-Kα radiation (graphite monochromator) with a frame time of 0.4 seconds and a detector distance of 4 cm.

Heat capacity measurements

Zero field heat capacity measurements were carried out on a single crystal of $YbZn_2GaO_5$ and a powder sample of $LuZn_2GaO_5$ using Helium-4 (1.8 K $\leq$ T $\leq$ 300 K) and dilution refrigeration (0.06 K $\leq$ T $\leq$ 2 K) set up attached to Quantum Design (QD) Physical Property Measurement System (PPMS). A representative single-crystal sample of $YbZn_2GaO_5$ mounted on a heat capacity measurement platform is shown in the supplementary information (see Fig. S3).

Magnetic measurements

Temperature-dependent magnetic susceptibility was measured using a 7 Tesla Cryogenic Ltd SQUID (superconducting quantum interference device) magnetometer with a Helium-3 probe from 0.3 K to 2 K and with a Helium-4 probe from 2 K to 300 K. For the Helium-3 measurements, a small crystalline $YbZn_2GaO_5$ sample of 1.04 mg was mounted on a silver sample holder and the Helium-4 measurement, 11.90 mg of $YbZn_2GaO_5$ single crystal was used. The crystals were oriented using the Laue diffraction method and the regular shape of the single crystals was obtained using a wire saw. The magnetic measurements were performed under an applied magnetic field parallel ($H \| c$) and perpendicular ($H \perp c$) to the crystallographic c-directions of $YbZn_2GaO_5$. The isothermal magnetization measurements along both directions of $YbZn_2GaO_5$ single crystal sample were performed using a VSM (vibration sample magnetometer) in PPMS up to 14 Tesla of the applied magnetic field (see Fig. S1).

Inelastic neutron scattering

The inelastic neutron scattering (INS) experiments were performed on the Fine-Resolution Fermi Chopper Spectrometer (SEQUOIA) [40] and the Cold Neutron Chopper Spectrometer (CNCS) [41] at the Spallation Neutron Source (SNS), Oak Ridge National Laboratory. For the SEQUOIA experiment, 6.5 g of pure powder samples of $YbZn_2GaO_5$ and $LuZn_2GaO_5$ were used with incident neutron energies of

$E_i = 80$ and 120 meV at temperatures of $T = 5$ and 100 K. The phonon contributions in the $YbZn_2GaO_5$ spectrum were subtracted using isostructural non-magnetic $LuZn_2GaO_5$. For the CNCS experiment, 10 pieces of high-quality single crystal samples of $YbZn_2GaO_5$ with a total mass of ~ 1.8 g were co-aligned within 1.5° using a Laue X-ray back-scattering diffractometer and mounted along $(hk0)$ scattering plane on an oxygen-free copper sample holder (see Fig. S1). The measurements were carried out in a dilution refrigerator with a base temperature of 0.1 K. A neutron-absorbing Cd foil was placed at the bottom of the holder to reduce the background from the sample holder. The measurements were conducted at the base temperature and 45 K under zero-field with an incident neutron energy of E_i =3.32 meV. The sample was rotated with an increment of 1°, with a range of -180° to 180°. The data were analyzed using the HORACE software and were folded 3 times along the high symmetry axis $[0H0]$, $[\bar{H}H0]$, and $[H00]$ into a 60° sector in the reciprocal space to improve statistics. For the constant energy slice, the folded data were cut, duplicated, and recombined to restore 360° coverage for the purpose of presentation. To better extract the magnetic signal of interest, a comparative analysis was conducted between the 0.1 K and 45 K spectra. The 45 K spectrum was normalized to 0.1 K data and used as background which then was subtracted from the 0.1 K spectrum.

Theoretical calculations

We performed dynamical tensor network simulations of the $J_1 - J_2$ XXZ model on the triangular lattice, given by

$$H = J_1 \sum_{\langle i,j \rangle} \left(\Delta S_i^z S_j^z + S_i^x S_j^x + S_i^y S_j^y \right) \quad (1)$$

$$+ J_2 \sum_{\langle\langle i,j \rangle\rangle} \left(\Delta S_i^z S_j^z + S_i^x S_j^x + S_i^y S_j^y \right), \quad (2)$$

where S_i^α are spin-1/2 operators, and $\langle i,j \rangle$ and $\langle\langle i,j \rangle\rangle$ denote nearest- and next-nearest neighbor pairs, respectively. In this work, we only look at the value of $J_2/J_1 = 0.12$, which was chosen based on the similarity between the experimental spectra and the calculated spectra at this value reported in [28]. This value is believed to be deep in the QSL phase of the isotropic model [42]. To reflect some of the lowered symmetry in $YbZn_2GaO_5$, we add one anisotropy parameter Δ and study the Δ dependence; in principle, J_1 and J_2 could have different anisotropy parameters, and one could incorporate higher-order couplings as well, but the computational effort required to map the Brillouin zone for each choice of parameters means that we leave such further explorations for future work.

The quantity of interest is the dynamical structure factor, given by

$$S(\boldsymbol{q}, \omega) = \frac{1}{N} \sum_{\boldsymbol{x}} \int_0^\infty \frac{\mathrm{d}t}{2\pi} e^{i(\omega t - \boldsymbol{q}\cdot\boldsymbol{x})} G(\boldsymbol{x}, t), \quad (3)$$

with N the number of lattice sites. The quantity $G(\boldsymbol{x}, t)$ is the two-point spin-spin correlation function defined as

$$G(\boldsymbol{x}, t) = \langle \Omega | \, \boldsymbol{S}_x(t) \cdot \boldsymbol{S}_c(0) \, | \Omega \rangle \,, \quad (4)$$

where c denotes the center site of the lattice taken to be the origin, $\boldsymbol{x}$ is the distance of site $\boldsymbol{x}$ from the origin, and $|\Omega\rangle$ is the ground state of H with energy E_0. To calculate this quantity, we split the calculation into three parts by writing

$$\boldsymbol{S}_x \cdot \boldsymbol{S}_c = S_x^z S_c^z + \frac{1}{2} \left[S_x^+ S_c^- + S_x^- S_c^+ \right] \quad (5)$$

To calculate $S(\boldsymbol{q}, \omega)$, we use the same method described in Ref. 28, but we will provide a summary of the technique here.

First, we curl the triangular lattice into a cylinder with a circumference $C = 6$, and a length $L = 36$, such that $N = LC$, using the XC boundary conditions [43]. Then, working with matrix product states (MPS), we calculate the ground state using the density matrix renormalization group (DMRG) [44, 45]. The time evolution for $G(\boldsymbol{x}, t)$ is calculated using the time-dependent variational principle (TDVP) [46–50], with a time step of 0.1, and maximum time $T_{\max} = 30$. We use a maximum bond dimension $\chi = 512$ for the simulations.

To smooth the data in frequency space, we rescale $G(\boldsymbol{x}, t)$ by a Gaussian. In particular

$$G(\boldsymbol{x}, t) \longrightarrow e^{-\eta t^2} G(\boldsymbol{x}, t), \quad (6)$$

and we use $\eta = 0.02$ here. Since our system is inversion symmetric, we rewrite the Fourier transform in Eq. (3) as

$$S(\boldsymbol{q}, \omega) = \frac{1}{\pi N} \int_0^\infty \mathrm{d}t \sum\nolimits_{\boldsymbol{x}} \cos(\boldsymbol{q} \cdot \boldsymbol{x}) \times \Big(\cos(\omega t) \mathrm{Re} G(\boldsymbol{x}, t) - \sin(\omega t) \mathrm{Im} G(\boldsymbol{x}, t) \Big), \quad (7)$$

yielding the results displayed here.

Lastly, due to a small circumference of the cylinder used during the simulations, this restricts the allowed wavevectors $\mathbf{q}$ to a subset of the full Brillouin zone. Since the infinite system has a full C_6 rotational symmetry, this means that the dynamical structure factor should have the same symmetry. In particular, in the thermodynamic limit, for any rotation $R \in C_6$, we have

$$S(R\boldsymbol{q}, \omega) = S(\boldsymbol{q}, \omega). \quad (8)$$

We use this factor to generate the values $S(R\boldsymbol{q}, \omega)$ from the initial data $S(\boldsymbol{q}, \omega)$. For more details on the simulations, we point the reader to Ref. 28.

* equal contribution
† email:sara.haravifard@duke.edu

[1] L. Balents, Nature **464**, 199 (2010).
[2] P. W. Anderson, science **235**, 1196 (1987).

[3] A. Kitaev, Annals of Physics **303**, 2 (2003).
[4] P. Anderson, Materials Research Bulletin **8**, 153 (1973).
[5] L. Savary and L. Balents, Reports on Progress in Physics **80**, 016502 (2016).
[6] Y. Li, H. Liao, Z. Zhang, S. Li, F. Jin, L. Ling, L. Zhang, Y. Zou, L. Pi, Z. Yang, *et al.*, Scientific reports **5**, 16419 (2015).
[7] Y. Li, G. Chen, W. Tong, L. Pi, J. Liu, Z. Yang, X. Wang, and Q. Zhang, Phys. Rev. Lett. **115**, 167203 (2015).
[8] Y. Li, D. Adroja, P. K. Biswas, P. J. Baker, Q. Zhang, J. Liu, A. A. Tsirlin, P. Gegenwart, and Q. Zhang, Phys. Rev. Lett. **117**, 097201 (2016).
[9] Y. Shen, Y.-D. Li, H. Wo, Y. Li, S. Shen, B. Pan, Q. Wang, H. Walker, P. Steffens, M. Boehm, *et al.*, Nature **540**, 559 (2016).
[10] J. A. Paddison, M. Daum, Z. Dun, G. Ehlers, Y. Liu, M. B. Stone, H. Zhou, and M. Mourigal, Nature Physics **13**, 117 (2017).
[11] Z. Zhu, P. A. Maksimov, S. R. White, and A. L. Chernyshev, Phys. Rev. Lett. **119**, 157201 (2017).
[12] I. Kimchi, A. Nahum, and T. Senthil, Phys. Rev. X **8**, 031028 (2018).
[13] Y. Li, D. Adroja, R. I. Bewley, D. Voneshen, A. A. Tsirlin, P. Gegenwart, and Q. Zhang, Phys. Rev. Lett. **118**, 107202 (2017).
[14] Z. Ma, J. Wang, Z.-Y. Dong, J. Zhang, S. Li, S.-H. Zheng, Y. Yu, W. Wang, L. Che, K. Ran, S. Bao, Z. Cai, P. Čermák, A. Schneidewind, S. Yano, J. S. Gardner, X. Lu, S.-L. Yu, J.-M. Liu, S. Li, J.-X. Li, and J. Wen, Phys. Rev. Lett. **120**, 087201 (2018).
[15] M. M. Bordelon, E. Kenney, C. Liu, T. Hogan, L. Posthuma, M. Kavand, Y. Lyu, M. Sherwin, N. P. Butch, C. Brown, M. J. Graf, L. Balents, and S. D. Wilson, Nature physics **15**, 1058 (2019).
[16] L. Ding, P. Manuel, S. Bachus, F. Grußler, P. Gegenwart, J. Singleton, R. D. Johnson, H. C. Walker, D. T. Adroja, A. D. Hillier, and A. A. Tsirlin, Phys. Rev. B **100**, 144432 (2019).
[17] M. M. Bordelon, C. Liu, L. Posthuma, P. M. Sarte, N. P. Butch, D. M. Pajerowski, A. Banerjee, L. Balents, and S. D. Wilson, Phys. Rev. B **101**, 224427 (2020).
[18] J. Guo, X. Zhao, S. Ohira-Kawamura, L. Ling, J. Wang, L. He, K. Nakajima, B. Li, and Z. Zhang, Phys. Rev. Mater. **4**, 064410 (2020).
[19] K. M. Ranjith, D. Dmytriieva, S. Khim, J. Sichelschmidt, S. Luther, D. Ehlers, H. Yasuoka, J. Wosnitza, A. A. Tsirlin, H. Kühne, and M. Baenitz, Phys. Rev. B **99**, 180401 (2019).
[20] P.-L. Dai, G. Zhang, Y. Xie, C. Duan, Y. Gao, Z. Zhu, E. Feng, Z. Tao, C.-L. Huang, H. Cao, A. Podlesnyak, G. E. Granroth, M. S. Everett, J. C. Neuefeind, D. Voneshen, S. Wang, G. Tan, E. Morosan, X. Wang, H.-Q. Lin, L. Shu, G. Chen, Y. Guo, X. Lu, and P. Dai, Phys. Rev. X **11**, 021044 (2021).
[21] K. M. Ranjith, S. Luther, T. Reimann, B. Schmidt, P. Schlender, J. Sichelschmidt, H. Yasuoka, A. M. Strydom, Y. Skourski, J. Wosnitza, H. Kühne, T. Doert, and M. Baenitz, Phys. Rev. B **100**, 224417 (2019).
[22] Z. Zhang, X. Ma, J. Li, G. Wang, D. T. Adroja, T. P. Perring, W. Liu, F. Jin, J. Ji, Y. Wang, Y. Kamiya, X. Wang, J. Ma, and Q. Zhang, Phys. Rev. B **103**, 035144 (2021).
[23] Z. Zhang, J. Li, M. Xie, W. Zhuo, D. T. Adroja, P. J. Baker, T. G. Perring, A. Zhang, F. Jin, J. Ji, X. Wang, J. Ma, and Q. Zhang, Phys. Rev. B **106**, 085115 (2022).
[24] J. Xing, L. D. Sanjeewa, J. Kim, G. Stewart, M.-H. Du, F. A. Reboredo, R. Custelcean, and A. S. Sefat, ACS Materials Letters **2**, 71 (2019).
[25] A. O. Scheie, E. A. Ghioldi, J. Xing, J. A. M. Paddison, N. E. Sherman, M. Dupont, L. D. Sanjeewa, S. Lee, A. J. Woods, D. Abernathy, D. M. Pajerowski, T. J. Williams, S.-S. Zhang, L. O. Manuel, A. E. Trumper, C. D. Pemmaraju, A. S. Sefat, D. S. Parker, T. P. Devereaux, R. Movshovich, J. E. Moore, C. D. Batista, and D. A. Tennant, Witnessing quantum criticality and entanglement in the triangular antiferromagnet $kybse_2$ (2023), arXiv:2109.11527 [cond-mat.str-el].
[26] Y. Ran, M. Hermele, P. A. Lee, and X.-G. Wen, Phys. Rev. Lett. **98**, 117205 (2007).
[27] S. Hu, W. Zhu, S. Eggert, and Y.-C. He, Phys. Rev. Lett. **123**, 207203 (2019).
[28] N. E. Sherman, M. Dupont, and J. E. Moore, Phys. Rev. B **107**, 165146 (2023).
[29] M. Drescher, L. Vanderstraeten, R. Moessner, and F. Pollmann, Dynamical signatures of symmetry broken and liquid phases in an $s = 1/2$ heisenberg antiferromagnet on the triangular lattice (2022), arXiv:2209.03344 [cond-mat.str-el].
[30] Y. Zhou, K. Kanoda, and T.-K. Ng, Rev. Mod. Phys. **89**, 025003 (2017).
[31] Y.-D. Li and G. Chen, Phys. Rev. B **96**, 075105 (2017).
[32] Y. Shen, Y.-D. Li, H. C. Walker, P. Steffens, M. Boehm, X. Zhang, S. Shen, H. Wo, G. Chen, and J. Zhao, Nature Communications **9**, 4138 (2018).
[33] X.-G. Wen, Phys. Rev. B **65**, 165113 (2002).
[34] X.-Y. Song, C. Wang, A. Vishwanath, and Y.-C. He, Nature Communications **10**, 4254 (2019).
[35] Y. Xu, J. Zhang, Y. S. Li, Y. J. Yu, X. C. Hong, Q. M. Zhang, and S. Y. Li, Phys. Rev. Lett. **117**, 267202 (2016).
[36] E. Gopal, *Specific heats at low temperatures* (Springer Science & Business Media, 2012).
[37] R. Sarkar, P. Schlender, V. Grinenko, E. Haeussler, P. J. Baker, T. Doert, and H.-H. Klauss, Phys. Rev. B **100**, 241116 (2019).
[38] Z. Zhang, X. Ma, J. Li, G. Wang, D. T. Adroja, T. P. Perring, W. Liu, F. Jin, J. Ji, Y. Wang, Y. Kamiya, X. Wang, J. Ma, and Q. Zhang, Phys. Rev. B **103**, 035144 (2021).
[39] W. Steinhardt, P. Maksimov, S. Dissanayake, Z. Shi, N. P. Butch, D. Graf, A. Podlesnyak, Y. Liu, Y. Zhao, G. Xu, *et al.*, npj Quantum Materials **6**, 78 (2021).
[40] G. Granroth, A. Kolesnikov, T. Sherline, J. Clancy, K. Ross, J. Ruff, B. Gaulin, and S. Nagler, in *Journal of Physics: Conference Series*, Vol. 251 (IOP Publishing, 2010) p. 012058.
[41] G. Ehlers, A. A. Podlesnyak, J. L. Niedziela, E. B. Iverson, and P. E. Sokol, Review of Scientific Instruments **82**, 085108 (2011).
[42] Y. Iqbal, W.-J. Hu, R. Thomale, D. Poilblanc, and F. Becca, Phys. Rev. B **93**, 144411 (2016).
[43] A. Szasz, J. Motruk, M. P. Zaletel, and J. E. Moore, Phys. Rev. X **10**, 021042 (2020).
[44] S. R. White, Phys. Rev. Lett. **69**, 2863 (1992).
[45] U. Schollwöck, Annals of Physics **326**, 96 (2011), january 2011 Special Issue.
[46] J. Haegeman, J. I. Cirac, T. J. Osborne, I. Pižorn, H. Verschelde, and F. Verstraete, Phys. Rev. Lett. **107**, 070601 (2011).
[47] J. Haegeman, T. J. Osborne, and F. Verstraete, Phys. Rev. B **88**, 075133 (2013).
[48] J. Haegeman, C. Lubich, I. Oseledets, B. Vandereycken, and F. Verstraete, Phys. Rev. B **94**, 165116 (2016).
[49] L. Vanderstraeten, J. Haegeman, and F. Verstraete, SciPost Phys. Lect. Notes , 7 (2019).
[50] M. Yang and S. R. White, Phys. Rev. B **102**, 094315 (2020).

arXiv:2305.20040v1 [cond-mat.str-el] 31 May 2023

Supplementary information for 'Realization of U(1) Dirac Quantum Spin Liquid in $YbZn_2GaO_5$'

Sijie Xu,[1,*] Rabindranath Bag,[1,*] Nicholas E. Sherman,[2,3] Lalit Yadav,[1] Alexander I. Kolesnikov,[4] Andrey A. Podlesnyak,[4] Joel E. Moore,[2,3] and Sara Haravifard[1,5,†]

[1]*Department of Physics, Duke University, Durham, North Carolina 27708, USA*
[2]*Department of Physics, University of California, Berkeley, California 94720, USA*
[3]*Materials Sciences Division, Lawrence Berkeley National Laboratory, Berkeley, California 94720, USA*
[4]*Neutron Scattering Division, Oak Ridge National Laboratory, Oak Ridge, Tennessee 37831, USA*
[5]*Department of Mechanical Engineering and Materials Science, Duke University, Durham, North Carolina 27708, USA*

(Dated: June 1, 2023)

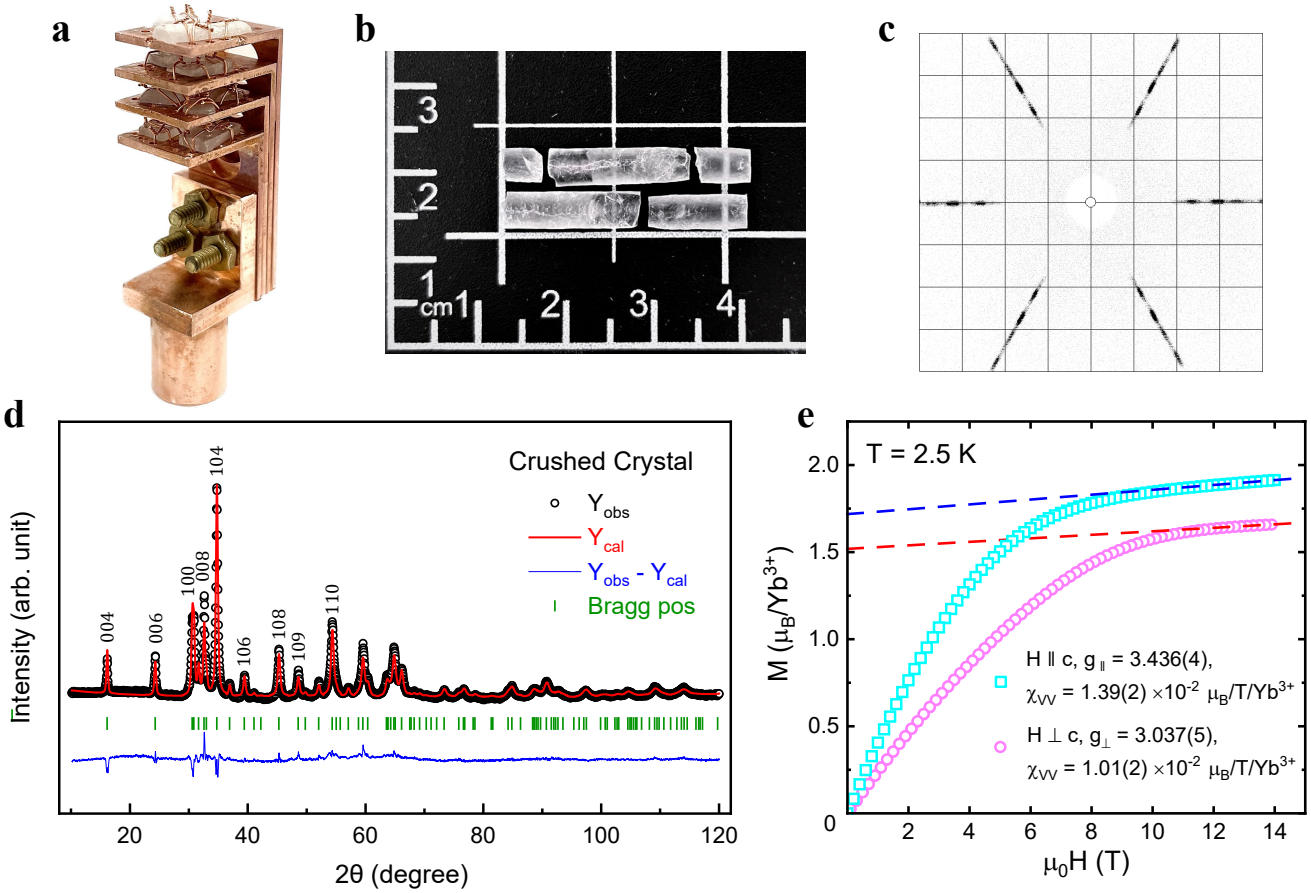

FIG. S1: **Pictures, Laue pattern, powder X-ray diffraction pattern, and isothermal magnetization**. **a**. A picture of co-aligned single crystals of $YbZn_2GaO_5$ on a neutron sample mount. 10 selected high-quality single crystals with a total mass of $\sim$ 1.8 grams were aligned and bound on an oxygen-free Cu sample mount with Cu wire. **b**. A representative image of the grown single crystals sample of $YbZn_2GaO_5$, the transparency of the crystal indicates its high quality. **c**. Sharp Laue Back-scattered X-ray pattern with an incident beam along the c-axis. **d**. Rietveld refinement performed on powder X-ray diffraction (PXRD) pattern of the ground single crystal of $YbZn_2GaO_5$. **e**. Field-dependent isothermal magnetization of $YbZn_2GaO_5$ single crystal collected at 2.5 K. The magnetic field was applied parallel and perpendicular to the crystallographic c-axis. The obtained gyromagnetic ratios g and Van-Vleck contribution χ_{VV} from the fit (red and blue dashed lines) are shown.

---

* equal contribution

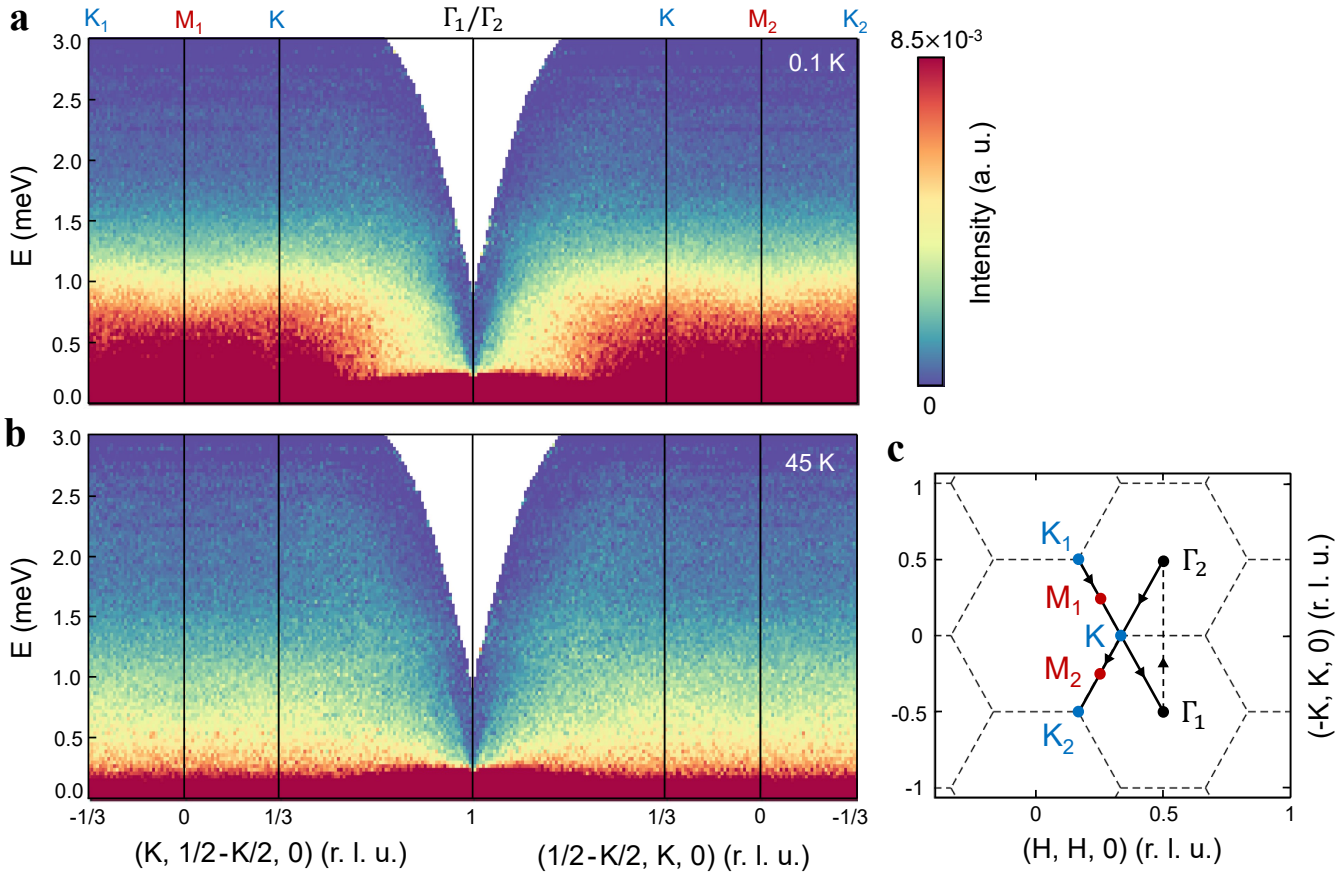

FIG. S2: **S(Q,ω) spectra at 0.1 K and 45 K, with E_i = 3.32 meV**. **a**. The raw intensity contour plot along high symmetry points measured at 0.1 K, with energy transfer on the y-axis and a reciprocal space path on the x-axis (as depicted in panel c). **b**. The raw intensity contour plot along the same path was obtained at a higher temperature 45 K. The 45 K spectrum was normalized to 0.1 data and subtracted as background from the 0.1 K spectrum (as illustrated in Fig. 3a of the paper). **c**. A schematic of the path used in a and b. The Brillouin zones' boundaries are indicated by dashed lines. The path travels through high symmetry points: K_1, M_1, K, Γ_1/Γ_2, K, M_2, K_2.

† email:sara.haravifard@duke.edu

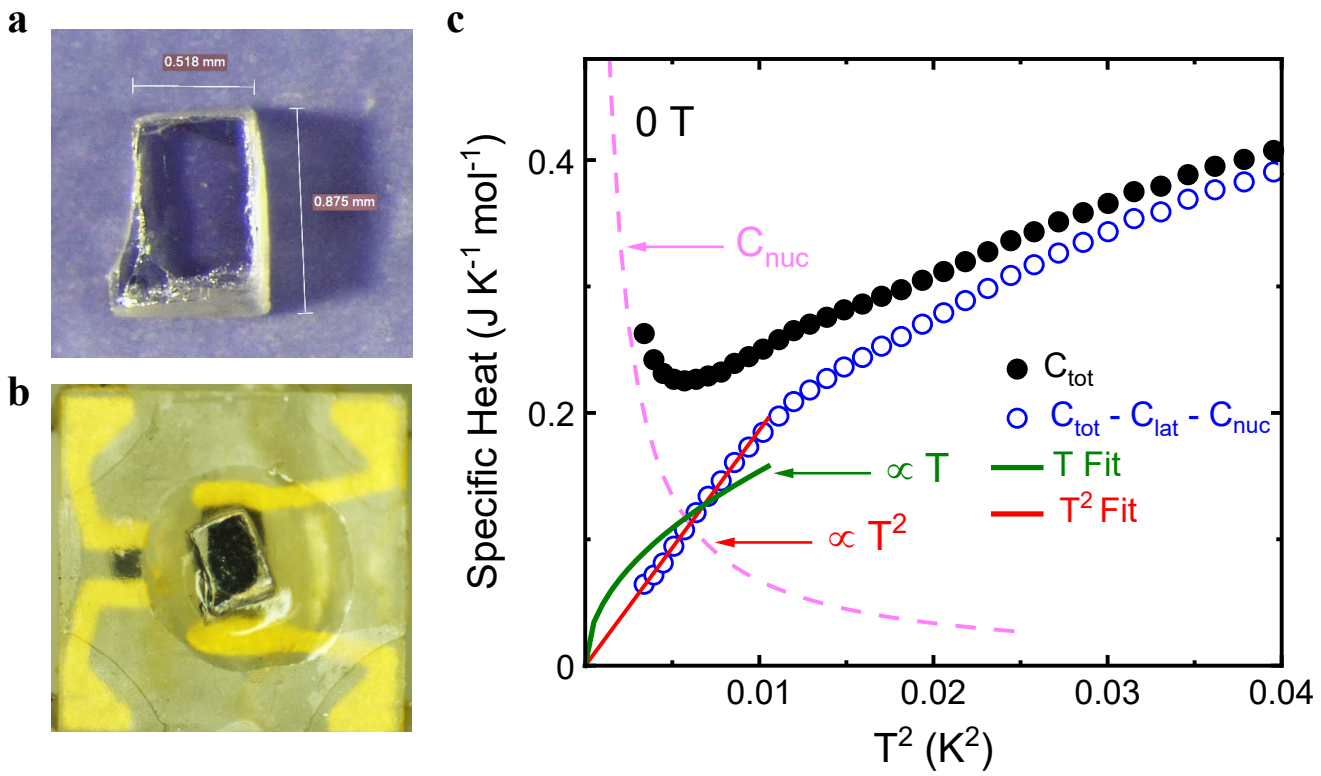

FIG. S3: **Heat capacity data fitted with linear and quadratic T models**. **a**. Microscopic image of $YbZn_2GaO_5$ single crystal sample used for heat capacity measurement. **b**. The mounted single crystal sample on a heat capacity platform of the Dilution Refrigerator set up of PPMS. The transparency of the single crystal sample of $YbZn_2GaO_5$ indicates the crystal quality. **c**. The filled black circles display the total heat capacity which can be written as $C_{tot} = C_{nuc} + C_{lat} + C_{mag}$. C_{nuc} is expressed as AT^{-2}; and C_{lat} is subtracted using the heat capacity of the non-magnetic $LuZn_2GaO_5$ sample. The light-magenta dash line indicates the nuclear contribution obtained from the fit. The blue circles show the data after subtracting the nuclear and lattice contribution. The green and red solid lines show the results of subtracted magnetic heat capacity data fitted using a linear (C_{mag} ∼T) and a quadratic (C_{mag} ∼T^2) models. The linear T dependence is expected for the spinon Fermi surface quantum spin liquid, while the quadratic behavior for T → 0 corresponds to U(1) Dirac quantum spin liquid model.

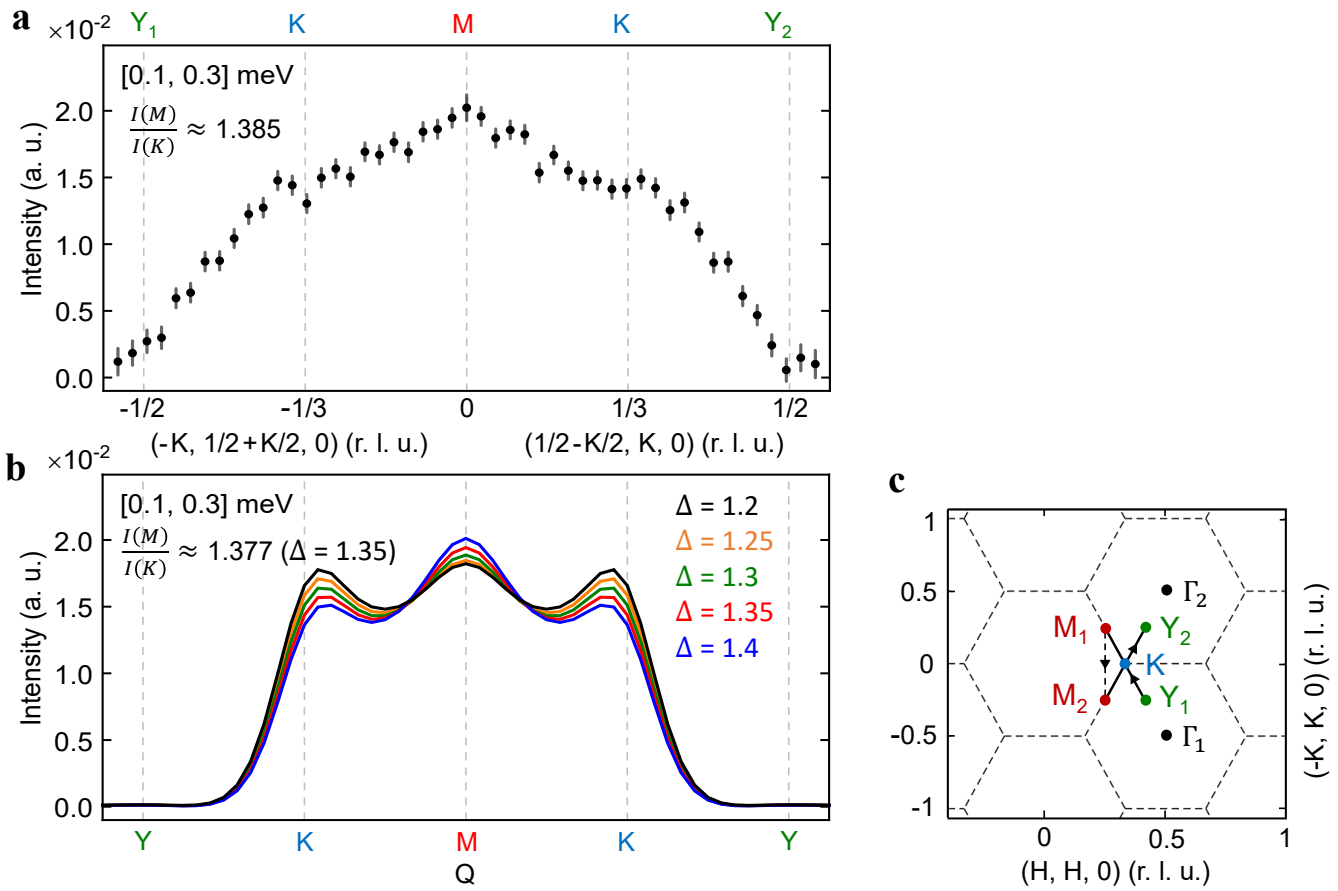

FIG. S4: **Line cut along high-symmetry points and theoretical calculation with different Δ values**. We present an investigation of the anisotropy effect in the low-energy INS spectrum. **a**. A line cut traveling through high symmetry points (as depicted in c.): Y_1, K, M_1/M_2, K, Y_2. The background-subtracted intensity was integrated between energy intervals [0.1, 0.3] meV and a small q window perpendicular to the high-symmetry path. The ratio of spectral weights between M and K points is around 1.385. **b**. Theoretical calculations of the spectral weights along the same path using different Δ values (Δ = 1.2, 1.25, 1.3, 1.35, 1.4). The ratios between spectral weights at the M and K points for different Delta were calculated, and we find that the ratio of the Δ = 1.35 case provides the best agreement with our experimental data. **c**. A schematic for the high symmetry path of the line cut is shown in a and b.

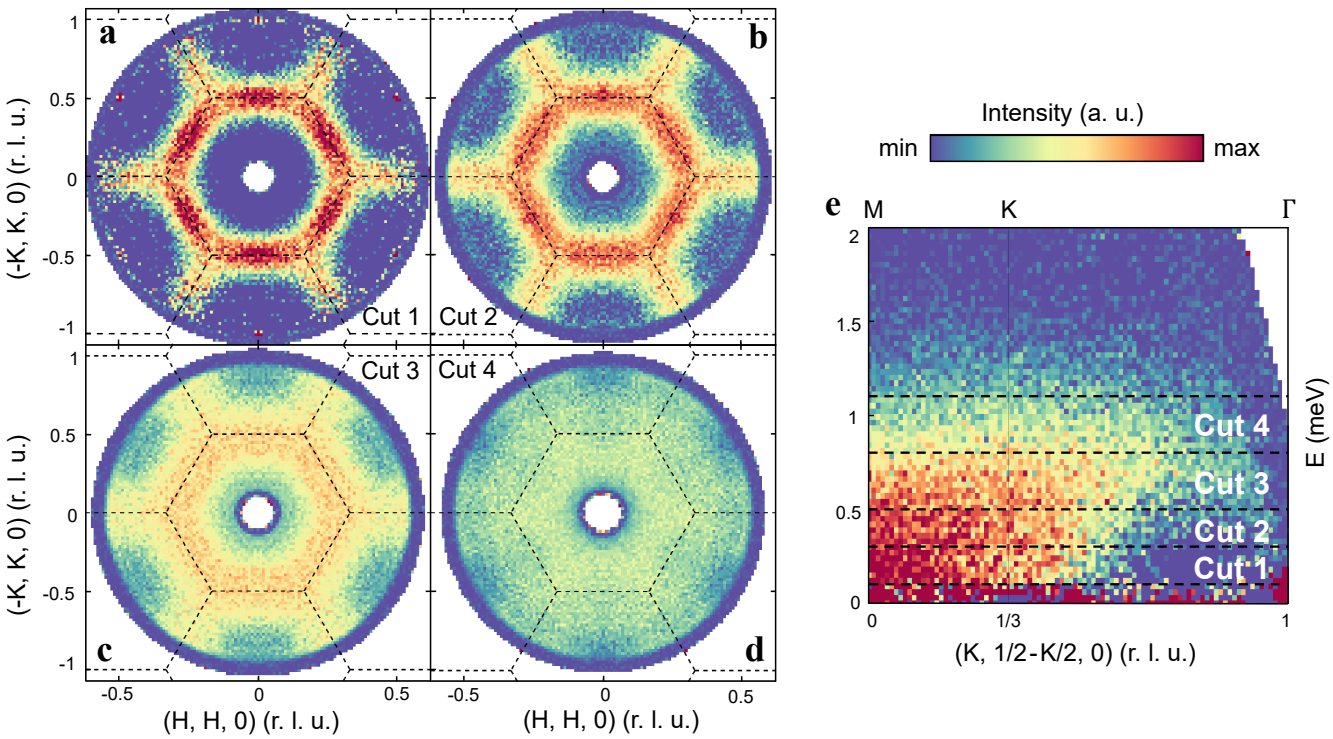

FIG. S5: **Momentum dependence of the magnetic excitation**. **a-d**. Background-subtracted constant energy slices of the magnetic excitation spectra collected at 0.1 K. The energy integration ranges are [0.1, 0.3], [0.3, 0.5], [0.5, 0.8], and [0.8, 1.1] meV. The spectra were folded along high symmetry directions to increase statistics and the folded data was duplicated and recombined to restore full coverage for presentation, as explained in the Methods section. The spectral weights are expressed by the same color map scale for better comparison. **e**. S(q,ω) plot along high symmetry path M-K-Γ. The dash lines indicate the energy integration intervals of cuts 1-4 for direct visualization.

TABLE S1: The refinement parameters of the single crystal X-ray diffraction (SCXRD) data collected at 150 K. The atomic coordinates and equivalent isotropic displacement parameters suggest no chemical site mixing in $YbZn_2GaO_5$. U(eq) is defined as one-third of the trace of the orthogonalized U^{ij} tensor.

$YbZn_2GaO_5$ SCXRD ($T = 150$ K, MoK_α, $\lambda = 0.71073$ Å)						
Space group	$P6_3mmc$ (No.194)					
Cell parameters	$a = b = 3.3678(2)$ Å, $c = 21.951(2)$ Å $\alpha = \beta = 90°$, $\gamma = 120°$					
Fit quality	$R1 = 0.0779$, $wR2 = 0.1895$, $GooF = 1.0612$					
Atom	**Site**	**x(Å)**	**y(Å)**	**z(Å)**	**U(eq)(Å^2)**	**Occ**
Yb1	$2a$	0.0000	0.0000	0.5000	0.0024	1.000
Ga1	$2b$	0.0000	0.0000	0.7500	0.0018	1.000
Zn1	$4f$	0.6667	0.3333	0.6372(1)	0.0018	1.000
O1	$4f$	0.6667	0.3333	0.5494(10)	0.00018	1.000
O2	$2c$	-0.3333	-0.6667	0.7500	0.0032	1.000
O3	$4e$	0.0000	0.0000	0.6546(11)	0.0020	1.000

TABLE S2: Fitted CEF parameters for $YbZn_2GaO_5$.

B_n^m	Fit values (meV)
B_0^2	-1.008×10^0
B_0^4	1.459×10^{-2}
B_3^4	-6.427×10^{-1}
B_0^6	5.446×10^{-4}
B_3^6	-3.284×10^{-2}
B_6^6	2.232×10^{-2}

TABLE S3: Eigenvalues and eigenvectors of the CEF Hamiltonian for $YbZn_2GaO_5$.

Eigenvalues (meV)	Eigenvectors
0.00	$-0.758\left\|-\frac{7}{2}\right\rangle + 0.402\left\|-\frac{1}{2}\right\rangle + 0.512\left\|\frac{5}{2}\right\rangle$
0.00	$-0.513\left\|-\frac{5}{2}\right\rangle + 0.402\left\|\frac{1}{2}\right\rangle + 0.758\left\|\frac{7}{2}\right\rangle$
38.14	$-0.834\left\|-\frac{5}{2}\right\rangle - 0.444\left\|\frac{1}{2}\right\rangle - 0.329\left\|\frac{7}{2}\right\rangle$
38.14	$-0.329\left\|-\frac{7}{2}\right\rangle + 0.444\left\|-\frac{1}{2}\right\rangle - 0.834\left\|\frac{5}{2}\right\rangle$
60.88	$\left\|-\frac{3}{2}\right\rangle$
60.88	$\left\|\frac{3}{2}\right\rangle$
94.00	$0.204\left\|-\frac{5}{2}\right\rangle - 0.801\left\|\frac{1}{2}\right\rangle + 0.563\left\|\frac{7}{2}\right\rangle$
94.00	$-0.563\left\|-\frac{7}{2}\right\rangle - 0.801\left\|-\frac{1}{2}\right\rangle - 0.204\left\|\frac{5}{2}\right\rangle$